

# $\phi^2$ FLIM: a technique for alias-free frequency domain fluorescence lifetime imaging

Alan D. Elder<sup>1</sup>, Clemens F. Kaminski<sup>1,2</sup>,  
and Jonathan H. Frank<sup>3,\*</sup>

<sup>1</sup>Department of Chemical Engineering, University of Cambridge, Cambridge, CB2 3RA, UK

<sup>2</sup>School of Advanced Optical Technologies, Max Planck Institute for the Science of Light,  
Guenther Scharowski Strasse 1, D-91058 Erlangen, Germany

<sup>3</sup>Combustion Research Facility, Sandia National Laboratories, Livermore, CA, 94551 USA  
[\\*jhfrank@sandia.gov](mailto:*jhfrank@sandia.gov)

**Abstract:** A new approach to alias-free wide-field fluorescence lifetime imaging in the frequency domain is demonstrated using a supercontinuum source for fluorescence excitation and a phase-modulated image intensifier for detection. This technique is referred to as phi-squared fluorescence lifetime imaging ( $\phi^2$ FLIM). The phase modulation and square-wave gating of the image intensifier eliminate aliasing by the effective suppression of higher harmonics. The ability to use picosecond excitation pulses without aliasing expands the range of excitation sources available for frequency-domain fluorescence lifetime imaging (fd-FLIM) and improves the modulation depth of conventional homodyne fd-FLIM measurements, which use sinusoidal intensity modulation of the excitation source. The  $\phi^2$ FLIM results are analyzed using AB-plots, which facilitate the identification of mono-exponential and multi-exponential fluorescence decays and provide measurements of the fluorophore fractions in two component mixtures. The rapid acquisition speed of the technique enables lifetime measurements in dynamic systems, such as temporally evolving samples and samples that are sensitive to photo-bleaching. Rapid  $\phi^2$ FLIM measurements are demonstrated by imaging the dynamic mixing of two different dye solutions at 5.5 Hz. The tunability of supercontinuum radiation enables excitation wavelength resolved FLIM measurements, which facilitates analysis of samples containing multiple fluorophores with different absorption spectra.

©2009 Optical Society of America

OCIS codes: (180.2520) Fluorescence microscopy; (170.3650) Lifetime-based sensing.

---

## References and links

1. A. D. Elder, A. Domin, G. S. Kaminski-Schierle, C. Lindon, J. Pines, A. Esposito, and C. F. Kaminski, "A quantitative protocol for dynamic measurements of protein interactions by FRET-sensitized fluorescence emission," *J. R. Soc. Interface* **6**, S59–S81 (2009).
2. A. Esposito, T. Tiffert, J. M. A. Mauritz, S. Schlachter, L. H. Bannister, C. F. Kaminski, V. L. Lew, and J. M. Schnur, "FRET imaging of hemoglobin concentration in Plasmodium falciparum-infected red cells," *PLoS ONE* **3**(11), e3780 (2008).
3. X. W. Dai, M. E. Eccleston, Z. L. Yue, N. K. H. Slater, and C. F. Kaminski, "A spectroscopic study of the self-association and inter-molecular aggregation behaviour of pH-responsive poly(L-lysine iso-phthalamide)," *Polymer (Guildf.)* **47**(8), 2689–2698 (2006).
4. J. R. Lakowicz, *Principles of Fluorescence Spectroscopy*, 2nd ed. (Plenum, New York, 1999).
5. S. M. Matthews, A. D. Elder, K. Yunus, C. F. Kaminski, C. M. Brennan, and A. C. Fisher, "Quantitative kinetic analysis in a microfluidic device using frequency-domain fluorescence lifetime imaging," *Anal. Chem.* **79**(11), 4101–4109 (2007).
6. A. Periasamy, P. Wodnicki, X. Wang, S. Kwon, G. Gordon, and B. Herman, "Time-resolved fluorescence lifetime imaging microscopy using a picosecond pulsed tunable dye laser system," *Rev. Sci. Instrum.* **67**(10), 3722–3731 (1996).

7. W. Becker, H. Hickl, C. Zander, K. H. Drexhage, S. S. M. Sauer, and J. Wolfrum, "Time-resolved detection and identification of single analyte molecules in microcapillaries by timecorrelated single-photon counting (TCSPC)," *Rev. Sci. Instrum.* **70**(3), 1835–1841 (1999).
8. J. R. Lakowicz, and K. W. Berndt, "Lifetime-selective fluorescence imaging using an rf phase-sensitive camera," *Rev. Sci. Instrum.* **62**(7), 1727–1734 (1991).
9. P. Schneider, and R. M. Clegg, "Rapid acquisition, analysis, and display of fluorescence lifetime-resolved images for real-time applications," *Rev. Sci. Instrum.* **68**(11), 4107 (1997).
10. J. R. Lakowicz, H. Szmajda, K. Nowaczyk, K. W. Berndt, and M. Johnson, "Fluorescence lifetime imaging," *Anal. Biochem.* **202**(2), 316–330 (1992).
11. T. W. J. Gadella, Jr., T. M. Jovin, and R. M. Clegg, "Fluorescence lifetime imaging microscopy (FLIM) - spatial resolution of microstructures on the nanosecond time-scale," *Biophys. Chem.* **48**(2), 221–239 (1993).
12. A. D. Elder, J. H. Frank, J. Swartling, X. Dai, and C. F. Kaminski, "Calibration of a wide-field frequency-domain fluorescence lifetime microscopy system using light emitting diodes as light sources," *J. Microsc.* **224**(2), 166–180 (2006).
13. A. Squire, P. J. Verveer, and P. I. H. Bastiaens, "Multiple frequency fluorescence lifetime imaging microscopy," *J. Microsc.* **197**(2), 136–149 (2000).
14. Q. S. Hanley, and A. H. A. Clayton, "AB-plot assisted determination of fluorophore mixtures in a fluorescence lifetime microscope using spectra or quenchers," *J. Microsc.* **218**(1), 62–67 (2005).
15. G. I. Redford, and R. M. Clegg, "Polar plot representation for frequency-domain analysis of fluorescence lifetimes," *J. Fluoresc.* **15**(5), 805–815 (2005).
16. M. A. Digman, V. R. Caiolfa, M. Zamai, and E. Gratton, "The phasor approach to fluorescence lifetime imaging analysis," *Biophys. J.* **94**(2), 14–16 (2008).
17. G. J. Kremers, E. B. van Munster, J. Goedhart, and T. W. J. Gadella, Jr., "Quantitative lifetime unmixing of multiexponentially decaying fluorophores using single-frequency fluorescence lifetime imaging microscopy," *Biophys. J.* **95**(1), 378–389 (2008).
18. S. Schlachter, A. D. Elder, A. Esposito, G. S. Kaminski, J. H. Frank, L. K. van Geest, and C. F. Kaminski, "mhFLIM: resolution of heterogeneous fluorescence decays in widefield lifetime microscopy," *Opt. Express* **17**(3), 1557–1570 (2009).
19. A. D. Elder, S. Schlachter, and C. F. Kaminski, "Theoretical investigation of the photon efficiency in frequency-domain fluorescence lifetime imaging microscopy," *J. Opt. Soc. Am. A* **25**(2), 452–462 (2008).
20. J. Philip, and K. Carlsson, "Theoretical investigation of the signal-to-noise ratio in fluorescence lifetime imaging," *J. Opt. Soc. Am. A* **20**(2), 368–379 (2003).
21. E. B. Van Munster, and T. W. J. Gadella, Jr., "phiFLIM: a new method to avoid aliasing in frequency-domain fluorescence lifetime imaging microscopy," *J. Microsc.* **213**(1), 29–38 (2004).
22. C. F. Kaminski, R. S. Watt, A. D. Elder, J. H. Frank, and J. Hult, "Supercontinuum radiation for applications in chemical sensing and microscopy," *Appl. Phys. B* **92**(3), 367–378 (2008).
23. J. H. Frank, A. D. Elder, J. Swartling, A. R. Venkitaraman, A. D. Jeyasekharan, and C. F. Kaminski, "A white light confocal microscope for spectrally resolved multidimensional imaging," *J. Microsc.* **227**(3), 203–215 (2007).
24. Q. S. Hanley, V. Subramaniam, D. J. Arndt-Jovin, and T. M. Jovin, "Fluorescence lifetime imaging: Multi-point calibration, minimum resolvable differences, and artifact suppression," *Cytometry* **43**(4), 248–260 (2001).
25. T. B. Settersten, A. Dreizler, and R. L. Farrow, "Temperature- and species-dependent quenching of CO B probed by two-photon laser-induced fluorescence using a picosecond laser," *J. Chem. Phys.* **117**(7), 3173–3179 (2002).
26. S. E. D. Webb, Y. Gu, S. Leveque-Fort, J. Siegel, M. J. Cole, K. Dowling, R. Jones, P. M. W. French, M. A. A. Neil, R. Juskaitis, L. O. D. Sucharov, T. Wilson, and M. J. Lever, "A wide-field time-domain fluorescence lifetime imaging microscope with optical sectioning," *Rev. Sci. Instrum.* **73**(4), 1898–1907 (2002).
27. C. Dunsby, P. M. P. Lanigan, J. McGinty, D. S. Elson, J. Requejo-Isidro, I. Munro, N. Galletly, F. McCann, B. Treanor, B. Onfelt, D. M. Davis, M. A. A. Neil, and P. M. W. French, "An electronically tunable ultrafast laser source applied to fluorescence imaging and fluorescence lifetime imaging microscopy," *J. Phys. D Appl. Phys.* **37**(23), 3296–3303 (2004).
28. R. K. P. Benninger, O. Hofmann, J. McGinty, J. Requejo-Isidro, I. Munro, M. A. A. Neil, A. J. Demello, and P. M. W. French, "Time-resolved fluorescence imaging of solvent interactions in microfluidic devices," *Opt. Express* **13**(16), 6275–6285 (2005).
29. D. S. Elson, I. Munro, J. Requejo-Isidro, J. McGinty, C. Dunsby, N. Galletly, G. W. Stamp, M. A. A. Neil, M. J. Lever, P. A. Kellet, A. Dymoke-Bradshaw, J. Hares, and P. M. W. French, "Real-time time-domain fluorescence lifetime imaging including single-shot acquisition with a segmented optical image intensifier," *N. J. Phys.* **6**, 180–192 (2004).
30. K. K. Sharman, A. Periasamy, H. Ashworth, J. N. Demas, and N. H. Snow, "Error analysis of the rapid lifetime determination method for double-exponential decays and new windowing schemes," *Anal. Chem.* **71**(5), 947–952 (1999).
31. O. Holub, M. J. Seufferheld, C. Gohlke, Govindjee, and R. M. Clegg, "Fluorescence lifetime imaging in real-time - a new technique in photosynthesis research," *Photosynthetica* **38**(4), 581–599 (2000).

---

## 1. Introduction

Fluorescence lifetime imaging (FLIM) provides spatially resolved quantitative measurements of excited state lifetimes of fluorophores. The fluorescence lifetime is a sensitive indicator of

the local molecular environment. FLIM measurements can probe molecular interactions, such as fluorescence resonance energy transfer (FRET) [1-2], molecular conformation [3], pH, the presence of quenchers such as dissolved oxygen, the presence of ions such as  $[Ca^{2+}]$  [4], and the kinetics of chemical reactions [5]. There is a great demand for new FLIM techniques that probe complex environments with increased accuracy over shorter measurement time scales.

Fluorescence lifetime measurements can be performed in either the time domain [6-7] or the frequency domain [8-9]. For time-domain measurements, the sample is excited with a short pulse of light, and the resulting fluorescence decay is sampled as a function of time. Conventionally, a single-exponential decay is fitted to the time-sampled data. However, single-exponential fits have a limited use since many fluorophores have multi-exponential decays, and many samples contain mixtures of fluorophores with different lifetimes. The separation of components of a multi-exponential decay requires data with a high signal-to-noise ratio. The ability to resolve multiple exponential decays also depends on the instrument response function of the detection system and the difference between the lifetimes of the fluorophores. For frequency-domain measurements, the intensity of the excitation source is periodically modulated. The resulting fluorescence emission is phase shifted and demodulated relative to the excitation source. The fluorescence lifetime is determined from the phase shift ( $\phi$ ) and modulation depth ( $m$ ), which are measured using either a homodyne or heterodyne detection scheme [4, 10–12]. If the fluorescence decay is single-exponential, the phase and modulation lifetimes will be identical. Multi-exponential decays can be determined by taking measurements at several different modulation frequencies and fitting a multi-exponential model to the data [4, 13]. Recently, an alternative technique referred to as the *AB*-plot analysis [14] has been introduced (also referred to as a polar plot [15] or a phasor plot [16]), which has significant benefits for the analysis of multi-exponential decays [17-18]. Here the wide-field frequency-domain implementation of FLIM is considered, and data analysis is presented in terms of the *AB*-plot technique.

### 1.1 Wide-field frequency-domain FLIM

Wide-field frequency-domain FLIM measurements use a micro-channel plate (MCP) intensified CCD camera for fluorescence detection, the gain of which is modulated by modulating the voltage applied to the photo-cathode. The illumination is provided by an intensity-modulated light source, such as a light emitting diode, pulsed laser, or a cw laser with an acousto-optic modulator. The phase shift and demodulation are usually measured using a homodyne detection scheme, in which the gain and excitation waveforms are modulated at precisely the same frequency. By acquiring a series of measurements at different relative phase offsets between the excitation and gain modulation waveforms, the lifetime can be determined by either a Fourier analysis or a linear least squares fit to a phase-shifted and demodulated sinusoid [12]. In the case of evenly distributed phase steps, these methods are equivalent. Traditionally, only data from the fundamental harmonic is analyzed, although the lifetime can also be calculated from higher harmonics, if they are present in the detected signal.

For a linear least squares fit to the fundamental frequency, the detected waveform is fit to a function of the form of Eq. (1).

$$y_i = a_1 + a_2 \cos(\phi_i^g - a_3) \quad (1)$$

where  $y$  is the measured signal,  $\phi_i^g$  is the phase offset of the gain waveform,  $a_1$ ,  $a_2$  and  $a_3$  are fitting parameters, and  $i$  refers to the measurement at the  $i^{\text{th}}$  phase step. As shown in Ref [19], the least squares fitting parameters,  $\theta_1$ ,  $\theta_2$  and  $\theta_3$  are given by

$$\theta_1 = \frac{1}{N} \sum_{i=1}^N y_i \quad (2)$$

$$\theta_2 = \frac{2}{N} \sum_{i=1}^N y_i \cos(\phi_i^g) \quad (3)$$

$$\theta_3 = \frac{2}{N} \sum_{i=1}^N y_i \sin(\phi_i^g) \quad (4)$$

where

$$\theta_1 = a_1 \quad (5)$$

$$\theta_2 = a_2 \cos(a_3) \quad (6)$$

$$\theta_3 = a_2 \sin(a_3) \quad (7)$$

A reference measurement of a sample with a known lifetime is used to account for the inherent phase shift and demodulation of the electronics and optics. The fluorescence lifetime is determined from the phase shift and the demodulation using Eqs. (8) and (9), respectively [12].

$$\tau_\phi = \frac{1}{\omega} \tan \left( \arctan \left( \frac{\theta_3}{\theta_2} \right) - \arctan \left( \frac{\theta_{3,ref}}{\theta_{2,ref}} \right) + \arctan \left( \omega \tau_{ref} \right) \right) \quad (8)$$

$$\tau_m = \frac{1}{\omega} \left( \left( \frac{\theta_{2,ref}^2 + \theta_{3,ref}^2}{\theta_{1,ref}^2} \right) \left( \frac{\theta_1^2}{\theta_2^2 + \theta_3^2} \right) (1 + \omega^2 \tau_{ref}^2) - 1 \right)^{\frac{1}{2}} \quad (9)$$

$\omega$  is the angular modulation frequency,  $\tau$  is the lifetime, the subscript  $\phi$  refers to the phase lifetime, the subscript  $m$  refers to the modulation lifetime, and the subscript *ref* refers to the reference measurement.

### 1.2 AB imaging

We present our analysis in terms of *AB*-plots [14]. The *AB*-plot is a powerful technique for quantitative analysis and visualization of lifetime data, especially for fluorophores that have multi-exponential lifetime decays. This technique plots data points using *A*- and *B*-coordinates defined by  $A = m \sin(\phi)$  and  $B = m \cos(\phi)$ . Since  $m$  and  $\phi$  are determined in frequency-domain FLIM measurements, the technique is ideally suited to frequency-domain data analysis. The *A* and *B* parameters can be determined from the least squares fitting parameters,  $\theta_1$ ,  $\theta_2$  and  $\theta_3$ , according to Eqs. (10) and (11).

$$A = \frac{\theta_3}{\theta_1} \quad (10)$$

$$B = \frac{\theta_2}{\theta_1} \quad (11)$$

As in the case of the phase and modulation lifetime, a reference measurement is used to account for demodulations and delays due to the optics and electronics. In this case the *A* and *B* parameters are given by Eqs. (12) and (13).

$$A = \frac{1}{\theta_1} \left( \frac{-a_{1,ref} \sin(a_{3,ref} - \arctan(\omega\tau_{ref}))}{a_{2,ref} (1 + \omega^2\tau_{ref}^2)^{0.5}} \theta_2 + \frac{a_{1,ref} \cos(a_{3,ref} - \arctan(\omega\tau_{ref}))}{a_{2,ref} (1 + \omega^2\tau_{ref}^2)^{0.5}} \theta_3 \right) \quad (12)$$

$$B = \frac{1}{\theta_1} \left( \frac{a_{1,ref} \cos(a_{3,ref} - \arctan(\omega\tau_{ref}))}{a_{2,ref} (1 + \omega^2\tau_{ref}^2)^{0.5}} \theta_2 + \frac{a_{1,ref} \sin(a_{3,ref} - \arctan(\omega\tau_{ref}))}{a_{2,ref} (1 + \omega^2\tau_{ref}^2)^{0.5}} \theta_3 \right) \quad (13)$$

where  $a_{1,ref}$ ,  $a_{2,ref}$  and  $a_{3,ref}$  are the reference fitting parameters.

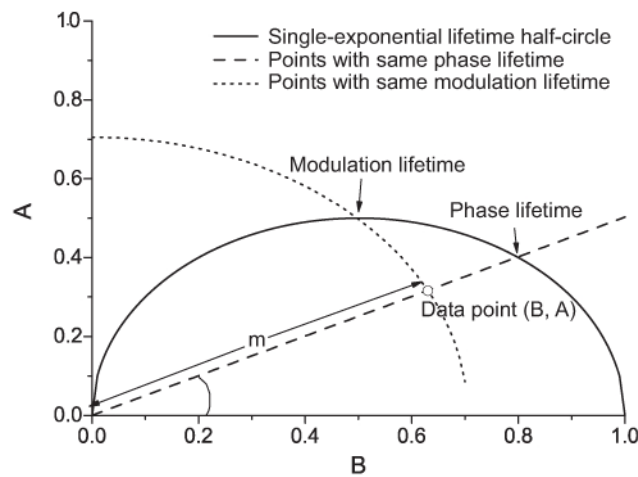


Fig. 1.  $AB$ -plot demonstrating the relationship between a data point in  $AB$  space and the phase and modulation lifetimes.

Figure 1 shows the relationship between mono-exponential and multi-exponential decays on an  $AB$ -plot. For mono-exponential decays, the  $AB$  coordinates lie on a semi-circle that intersects the points (0.0,0.0), (0.5, 0.5) and (1.0, 0.0) [15]. Shorter lifetimes are located further from the origin along the semi-circle. For a multi-exponential decay, the data points lie within the semi-circle. In certain cases, such as systems with FRET, the data points can lie outside of the semi-circle. When data points are not from mono-exponential decays, the phase and modulation lifetimes are different, as illustrated in Fig. 1

If a sample consists of two fluorophores with different lifetime components, then the  $AB$ -plot of the mixture lies on the straight line between the points corresponding to the two individual components. The vector from the origin to the data point for the mixture is equal to the sum of vectors of the individual components. The fraction of each component is given by the relative distance along the line. This relationship is particularly useful in analyzing fluorophore mixtures because it applies regardless of whether the two components have mono- or multi-exponential decays. This is demonstrated in Fig. 2.

If a system consists of two fluorophores with bi-exponential decays, the fractional contribution of each fluorophore to the fluorescence signal can be determined using vector addition with an  $AB$ -plot, provided that the  $AB$  coordinates for the individual fluorophores can be determined. In contrast, the traditional approach to analyzing such a mixture requires

resolving four different exponential decays to determine the relative amounts of each component. As demonstrated in Fig. 1, the phase and modulation lifetimes are 1-D projections of the 2-D  $AB$  data. Because of the nature of this projection, the phase and modu-

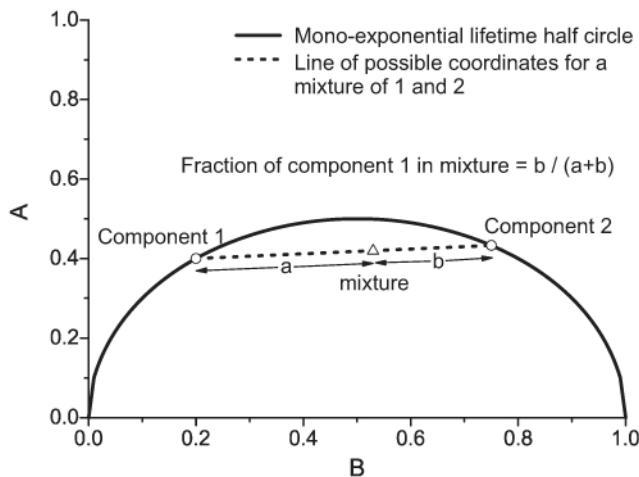


Fig. 2.  $AB$ -plot showing the possible  $AB$  coordinates for a two component mixture.

ulation lifetimes are very sensitive to uncertainties in the  $AB$  coordinates over certain regions of the  $AB$ -plot. As  $B$  approaches 1.0, a small change in either  $A$  or  $B$  leads to a large change in the modulation lifetime. For example, a shift from the point (0.98,0.14) on the semi-circle of mono-exponential decay to the point (0.97,0.14), just inside the semi-circle, changes the modulation lifetime from 0.56 ns to 0.79 ns, when using a 40 MHz modulation frequency. If the measured sample contains a distribution of fluorescence lifetimes, the non-linear nature of the projection in this region of the  $AB$ -plot causes the mean modulation lifetime to be biased towards higher values [12].

### 1.3 Aliasing

Accurate frequency-domain fluorescence lifetime measurements require sampling the phase steps at a frequency that is greater than the Nyquist frequency. Insufficient sampling introduces artifacts and leads to an erroneous reconstruction of the signal, which is referred to as aliasing. According to Nyquist sampling theory, measurements of frequencies greater than, or equal to, half the sampling frequency suffer from aliasing.

For frequency-domain FLIM measurements, the detected signal only contains higher harmonics that are present in both the excitation and detection waveforms [19]. If either the excitation or gain waveforms are pure sine functions, the detected signal contains only the fundamental frequency, and aliasing is not a problem. Since the gain of an image intensifier is a highly non-linear function of the applied voltage, the application of a smoothly varying periodic waveform results in a gain waveform that has abrupt transitions with high harmonic content [13]. Therefore, the detection system inherently contains multiple higher harmonics, and the elimination of harmonics in the FLIM signal requires sinusoidal modulation of the excitation source. Sinusoidal excitation is feasible using a modulated light-emitting diode (LED) or an acousto-optic modulator (AOM) coupled with a CW excitation source. However, previous studies have demonstrated that excitation with a Dirac delta function provides optimal signal-to-noise ratios for frequency-domain fluorescence lifetime measurements [19-20]. The combination of a Dirac delta function for fluorescence excitation and an image intensifier for detection produces a signal that contains many higher harmonics. The higher harmonic content can be beneficial because it enables the analysis of multiple frequencies from a single measurement [13, 18]. However, the higher harmonics can introduce artifacts from aliasing, which leads to erroneous lifetime measurements.

The problem of aliasing in homodyne detection fd-FLIM measurements can be solved in two ways. Either the number of sampled phase steps can be increased such that all significant harmonic contributions are resolved, or the detection scheme can be modified to suppress the higher harmonics. The former approach is often impractical because of measurement time constraints, such as sample movement or photobleaching. There is currently only one published method for eliminating aliasing from fd-FLIM measurements that use excitation and gain waveforms with multiple harmonics. This method was demonstrated using fluorescence lifetime imaging microscopy and is referred to as  $\phi$ FLIM [21]. The  $\phi$ FLIM technique eliminates aliasing by phase modulating the image intensifier gain waveform to rapidly sample multiple phase steps without requiring an increase in the framing rate of the CCD camera. A single frame measures the integrated signal over all phases, instead of each phase step requiring a separate image, as is the case in traditional fd-FLIM measurements. In  $\phi$ FLIM, the relative contribution of each phase to the integrated signal can be weighted by varying the rate of change of the phase. The phase modulation waveform is chosen judiciously such that the weighting of each phase step is the same as that used in linear least squares fitting. By using three different modulation waveforms and acquiring an image with each, the authors of Ref [21]. obtained integrated signals that were equivalent to the three least squares fitting parameters  $\theta_1$ ,  $\theta_2$  and  $\theta_3$ , in Eqs. (2-4). Since the phase modulation was performed using a programmable arbitrary waveform generator with thousands of phase steps, each of these fitting parameters was measured with a very high effective sampling rate, and aliasing was eliminated from the resulting fluorescence lifetime measurement.

However, the data presented in Ref [21]. indicate that the  $\phi$ FLIM method suffers from considerably more noise than the conventional approach to fd-FLIM, in which measurements are acquired at a series of distinct phase steps. For example, a 256 x 256 pixel FLIM image in Ref [21]. had a standard deviation in the measured phase angle that was on the order of 10 degrees. For a fluorescence lifetime of 3.0 ns and a modulation frequency of 75 MHz, a phase angle error of  $\pm 10$  degrees corresponded to a shift in the measured lifetime from approximately 2.1 to 4.5 ns, giving an uncertainty of  $-30\%$  to  $+50\%$ .

There are two central factors that contribute to the high noise levels in the  $\phi$ FLIM measurements. First, the use of only three images for determining fluorescence lifetimes is inherently noisier than conventional fd-FLIM, which uses a larger series of images that are acquired at many individual phase steps. Another factor is the method by which  $\phi$ FLIM images are collected. In order to mimic the linear least squares fitting with phase modulation of the intensifier gain, the signal at each phase is weighted by values of 1,  $\cos(\phi_g)$ , and  $\sin(\phi_g)$  to obtain the three least squares fitting parameters  $\theta_1$ ,  $\theta_2$  and  $\theta_3$ . Over a 360 degree range, these weighting factors include negative values. For conventional fd-FLIM, negative weighting coefficients are not an issue because the integration is performed in software. In  $\phi$ FLIM, however, the integration is performed during the image collection process, and it is impossible to achieve negative weighting coefficients. The authors of Ref [21]. circumvented this issue by adding an offset of 1.0 to the two phase modulation functions with negative values. The resulting weighting functions for the three images were 1.0,  $1.0 + \cos(\phi_g)$  and  $1.0 + \sin(\phi_g)$ . The recorded signals were thus equivalent to  $\theta_1$ ,  $\theta_1 + \theta_2$  and  $\theta_1 + \theta_3$ , from which  $\theta_1$ ,  $\theta_2$  and  $\theta_3$  were calculated. However, the use of this offset reduces the modulation depth of the intensifier gain waveform by 50%. A decrease in the modulation depth effectively reduces the dynamic range of the measurement, resulting in fluorescence lifetime measurements with greater noise [19].

#### 1.4 Phi-squared fluorescence lifetime imaging microscopy ( $\phi^2$ FLIM)

We present a new method to eliminate aliasing from FD-FLIM measurements using a combination of phase modulation and a judicious choice of the intensifier gain waveform that

improves the effective dynamic range of the detection. We refer to this method as phi-squared fluorescence lifetime imaging microscopy ( $\phi^2$ FLIM). This method provides alias-free wide-field FLIM measurements using Dirac delta excitation waveforms in conjunction with square-wave gating of an image intensifier. The theoretical basis for  $\phi^2$ FLIM is described in Section 2 and is followed by an experimental demonstration using a supercontinuum source for fluorescence excitation. The  $\phi^2$ FLIM results are compared with highly-resolved conventional homodyne FLIM measurements to evaluate the degree of aliasing. The essence of  $\phi^2$ FLIM is to superimpose a phase modulation on the detector gain such that all higher harmonic frequencies in the signal are suppressed. The resulting sinusoidal signal waveform can be accurately sampled with as few as three phase steps. The  $\phi^2$ FLIM measurements have a significantly higher signal-to-noise ratio than the  $\phi$ FLIM results in Ref [21]. The use of supercontinuum radiation for excitation enables excitation-wavelength resolved *AB* imaging, and we demonstrate measurements at rates of 5.5 Hz.

## 2. Theory

In this section, the theoretical basis of  $\phi^2$ FLIM is presented using fluorescence excitation pulses that are Dirac delta functions and an intensifier gain waveform that can be expressed as the sum of a series of sine waves. For this combination of waveforms, the detected signal at phase step *i* is given by Eq. (14) [19].

$$X_i = a + \sum_{j=1}^J \frac{b_j \cos(j\phi_i^g - \xi_j)}{(1+(j\omega\tau)^2)^{\frac{1}{2}}} \quad (14)$$

where *a* is the dc-component of the gain waveform, *b* is the amplitude of the gain waveform, *J* is the number of harmonics present in the gain waveform, the subscript *j* refers to the *j*th harmonic component.  $\xi_j$  is the phase shift of the *j*th harmonic component and is given by  $\xi_j = \arctan(-1/(j\omega\tau))$ .

In conventional homodyne detection, the fluorescence signal  $X_i$  is measured at a series of fixed phase steps, and this series of measurements is used to determine the fluorescence lifetime. However, the  $\phi^2$ FLIM technique uses a modulated phase delay, and the detected signal is given by the integral over one period of modulation. We choose the modulation signal to be  $\arccos(1-\psi)$  for  $\psi = 0$  to  $\psi = 2$ . This modulation function provides a sinusoidal weighting coefficient of the fluorescence signals from different phases. To avoid a large discontinuity in the repeated waveform, the waveform is followed by its mirror image for values of  $\psi$  from 2 to 4, as shown in Fig. 3.

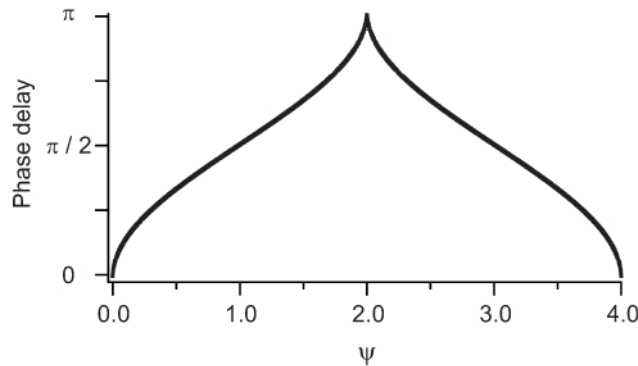


Fig. 3. The phase modulation applied to the detector gain waveform for  $\phi^2$ FLIM measurements.

The detected signal is then given by

$$X_i = \int_0^2 \left( a + \sum_{j=1}^J \frac{b_j \cos(j(\phi_i^g + \arccos(1-\psi)) - \xi_j)}{(1+(j\omega\tau)^2)^{\frac{1}{2}}} \right) d\psi \quad (15)$$

A substitution of variables using the expression  $\psi = 1 - \cos(\gamma)$  in Eq. (15) gives

$$X_i = \int_0^\pi \left( a + \sum_{j=1}^J \frac{b_j \cos(j\gamma + (j\phi_i^g - \xi_j))}{(1+(j\omega\tau)^2)^{\frac{1}{2}}} \right) \sin(\gamma) d\gamma \quad (16)$$

Thus the chosen modulation signal leads to a sinusoidal weighting of each phase step measurement. Equation (16) can be rewritten using standard trigonometric identities and integrating to give

$$X_i = 2a - \left[ \left( \frac{b_1\pi}{2} \right) \left( \frac{1}{1+(\omega\tau)^2} \right)^{\frac{1}{2}} \sin(\phi_i^g - \xi_1) \right] + \sum_{\text{even } j}^J \left[ \left( \frac{-2b_j}{j^2-1} \right) \left( \frac{1}{1+(j\omega\tau)^2} \right)^{\frac{1}{2}} \cos(j\phi_i^g - \xi_j) \right] \quad (17)$$

Examination of Eq. (17) reveals that odd harmonics are eliminated by the integration, and only the fundamental frequency and the even harmonics remain. The even harmonics are attenuated by a factor proportional to  $1/(j^2-1)$ . However, the even harmonics can be eliminated by using a 50% duty-cycle square wave for the gain waveform. In this case, the modulation depths of all even harmonics,  $b_j$  for even  $j$ , are equal to zero. As a result, only the fundamental frequency contributes to the integrated signal, and Eq. (17) is reduced to

$$X_i = 2a - \left( \frac{b_1\pi}{2} \right) \left( \frac{1}{1+(\omega\tau)^2} \right)^{\frac{1}{2}} \sin(\phi_i^g - \xi_1)$$

This expression can be rearranged using standard trigonometric identities to give

$$X_i = 2a - \left( \frac{b_1\pi}{2} \right) \left( \frac{1}{1+(\omega\tau)^2} \right)^{\frac{1}{2}} \cos(\phi_i^g - \arctan(\omega\tau)) \quad (18)$$

The selected phase modulation and gain waveforms thus produce a demodulated signal that is a sinusoidal function of the phase step,  $\phi_i^g$ , without any higher harmonic contributions. The phase shift of the sinusoidal function is  $\omega\tau$  with only the fundamental harmonic present. The fluorescence lifetime is determined by fitting the signal to a sinusoidal function and using conventional single-frequency fd-FLIM analysis. The effects of aliasing are expected to be insignificant even when as few as three phase steps are used because only the fundamental harmonic is present. Note that a Fourier series analysis of a 50% duty cycle square wave leads

to  $a = 0.5$  and  $b_1 = 2/\pi$ . According to Eq. (18), the resulting maximum modulation depth is 1.0, which is twice that achievable for sinusoidal excitation [19].

### 3. Experimental method

An illustration of the experimental configuration for  $\phi^2$ FLIM measurements is shown in Fig. 4. The system consisted of a supercontinuum source (Fianium SC450) for fluorescence excitation and a fast-gated intensified CCD camera (Picostar HRI, LaVision) for detection. The supercontinuum laser operated at a repetition rate of 39.6 MHz with pulse widths on the order of 10 ps [22]. For the purposes of  $\phi^2$ FLIM, the excitation pulses were effectively Dirac delta functions because the pulse width was orders of magnitude shorter than both the period between the pulses and the fluorescence lifetimes of the fluorophores considered here.

A computer-controlled acousto-optic tunable filter (AOTF, Crystal Technology) was used to select a 1-2 nm bandpass from the visible region of the supercontinuum spectrum. The AOTF provided simultaneous electronic selection of excitation laser power and wavelength for up to 8 different wavelength bands, which facilitated measurements of fluorescence lifetimes as a function of excitation wavelength. In previous studies, we demonstrated the use of a supercontinuum laser and AOTF for fluorescence excitation scans in a confocal microscope [22-23].

The  $\phi^2$ FLIM system was configured for measurements of dye samples in a cuvette. The supercontinuum beam was expanded using a 3x telescope, and the expanded beam was focused into a sheet using a 300 mm focal length cylindrical lens. The dye cuvette was positioned at the beam waist such that a thin sheet of fluid next to the face of the cuvette was illuminated.

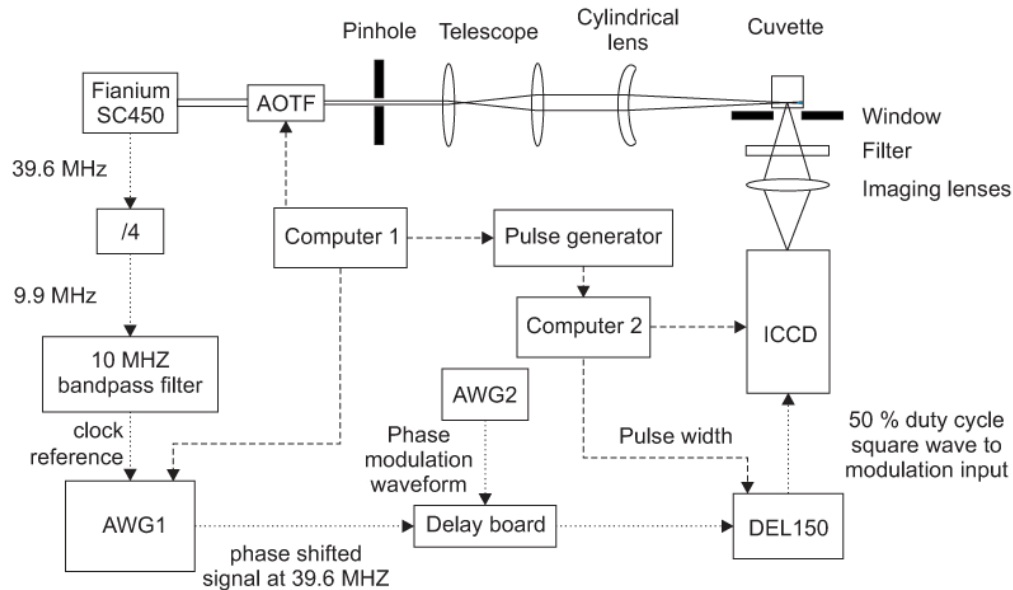


Fig. 4. Experimental configuration of the  $\phi^2$ FLIM system. SC450: supercontinuum source; AOTF: acousto-optic tunable filter; AWG: arbitrary waveform generator; ICCD: intensified charge-coupled device camera; DEL150: computer-controlled delay generator.

Fluorescence emission was imaged onto the intensified CCD camera using a pair of commercial camera lenses (Nikon 500 mm  $f/1.4$  and Nikon 105 mm  $f/4.5$ ). A long pass filter (Schott OG570) blocked elastic scattering of the laser light and transmitted the fluorescence emission. The gain on the intensified camera was modulated using an RF signal generator (Kentech HRI) to produce a 39.6 MHz square wave with the phase offset that was set using a high-precision computer-controlled delay module (DEL150, Becker and Hickl). The

harmonic content of the intensifier gain waveform was measured using elastic scattering of the supercontinuum laser pulses from a piece of ground glass. The signal from the scattered light was recorded as a function of the phase offset between the laser pulse train and the intensifier gain waveform using 72 phase steps. The harmonic content is plotted in Fig. 5. The fundamental frequency is the dominant component with contributions from odd higher harmonics decreasing as a function of the harmonic number. The modulation depth of the even harmonics is negligibly small.

A  $\phi^2$ FLIM measurement consists of a series of fluorescence images that are acquired at different phase offsets. Each image corresponds to the integrated signal given in Eq. (18). The number of phase offsets depends on the desired precision of the measurement. Two different

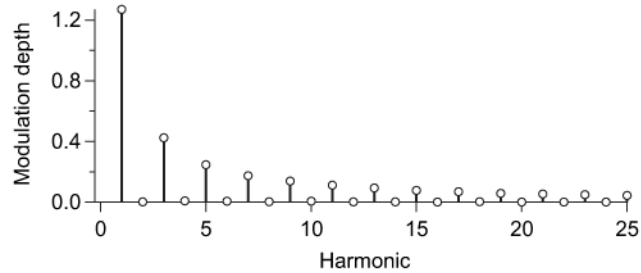


Fig. 5. Harmonic content of the intensifier gain waveform used for  $\phi^2$ FLIM. The data was obtained by measuring elastic scattering from a piece of ground glass at 72 different phase offsets.

methods for controlling the relative phases of the laser pulse train and the intensifier gain waveform are required. One method sets the phase offset for each image acquisition,  $\phi_i^g$ , and another modulates the phase according to the function given in Section 2. The phase offset was set using a computer-controlled arbitrary waveform generator (Agilent 33250A, AWG1 in Fig. 4) that was synchronized to the pulse-train of the supercontinuum laser. For synchronization, the 39.6 MHz pulse-train frequency was divided by four to generate a 9.9 MHz waveform as a clock reference for the arbitrary waveform generator.

The phase modulation of the intensifier gain waveform was produced using a voltage-controlled delay generator that was constructed from a voltage-to-time converter. The voltage-to-time converter consisted of a voltage ramping circuit that was triggered at a repetition rate of 39.6 MHz by the output of the arbitrary waveform generator. The converter produced a pulse each time the ramp voltage reached a user-selected threshold voltage, thus providing a 39.6 MHz pulse-train with a phase delay that was controlled by the threshold voltage. Modulation of the threshold voltage produced a phase modulated pulse train that triggered the DEL150 delay board. This delay board generated a square wave that was applied to the intensifier gain.

The waveform for phase modulation (see Fig. 3) was provided by a second arbitrary waveform generator (HP 33220A, AWG2 in Fig. 4). The period of the modulation waveform was equal to the integration time of the CCD camera, ensuring that every image had the desired phase weighting. In the experiments presented below, the phase was modulated at 2.5 Hz for an integration time of 400 ms. The system was easily adapted to perform conventional homodyne frequency-domain FLIM measurements by applying a constant threshold voltage to the voltage-to-time converter.

#### 4. Data analysis

The series of fluorescence images in a  $\phi^2$ FLIM measurement is analyzed on a pixel-by-pixel basis by fitting the fluorescence signal as a function of the phase step using a linear least squares fit to the expression in Eq. (1). The  $A$  and  $B$  parameters for each pixel are then calculated according to Eqs. (12) and 13.

Measurements of a reference sample with a known lifetime is required to account for the inherent phase shift produced by the collection optics and electronics. We use Rhodamine 6G (R6G) dye in a water solution with 0.2 M KCl as the reference sample. The fluorescence decay of this solution is mono-exponential with a lifetime of 4.0 ns, as shown in Section 5.1. The reference images of the fitting parameters,  $\theta_{1,ref}$ ,  $\theta_{2,ref}$  and  $\theta_{3,ref}$ , were smoothed using a 25x25-pixel boxcar average to reduce noise. The actual variation of the fitting parameters across the intensifier is very modest and is unaffected by the smoothing.

The results of the  $\phi^2$ FLIM measurements are plotted as distributions of points on an  $AB$  plot, from which fluorescence lifetimes are determined. If the decay is mono-exponential, the  $AB$  coordinate of each pixel can be projected onto the mono-exponential semi-circle. The average lifetime for a subregion of the image is calculated by averaging the modulation and phase lifetimes over multiple pixels. However, this approach can produce a biased average lifetime due to the projection of every point in  $AB$  space onto the mono-exponential semi-circle prior to computing the average. To eliminate this bias, we perform the averaging in  $AB$  space and then project the mean  $AB$  coordinate onto the closest point on the mono-exponential semi-circle. This method is illustrated in Fig. 6 and is referred to as the closest approach method. The uncertainty in the lifetime measurement is estimated by constructing a one standard deviation error region based on a bivariate normal distribution and then finding the closest point on the mono-exponential semi-circle to the extremities of the error region. The closest approach method of lifetime determination should only be used when a mono-exponential lifetime is expected, and the  $AB$  data points are in close proximity to the mono-exponential semi-circle, as is the case for R6G quenched by iodide ions.

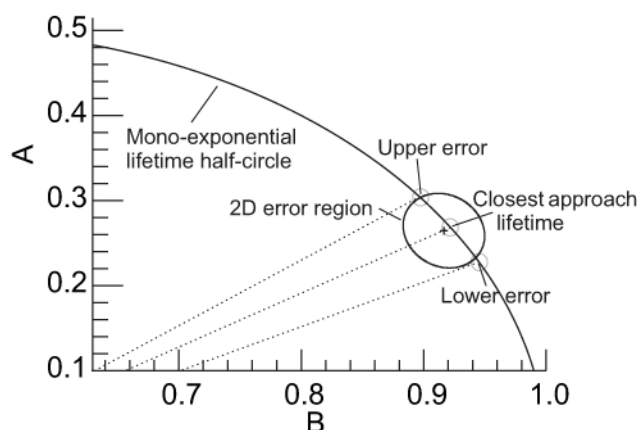


Fig. 6. Diagram illustrating the calculation of the closest approach mono-exponential lifetime and associated uncertainties. The closest point on the semi-circle to a given  $AB$  coordinate lies along a straight line between that coordinate and the point (0.5,0.0), as indicated by the dotted lines. The closest approach lifetime is calculated as the closest point on the semi-circle to the mean  $AB$  coordinate. The uncertainties are determined from the intersection of the one standard deviation region and the semi-circle.

## 5. Results

The phase-modulation fluorescence lifetime imaging system is demonstrated using solutions of Rhodamine 6G in water. The fluorescence lifetime of the R6G solution is varied by adding different concentrations of potassium iodide (KI) to change the quenching rate of the excited state. Figure 7 shows fluorescence signals as a function of phase offset for both the  $\phi^2$ FLIM technique and conventional homodyne detection for solutions with lifetimes of 3.6ns and 0.7ns. Each data set contains measurements at 72 phase steps with 5 degree phase increments. The fluorescence lifetimes can be accurately determined from the  $\phi^2$ FLIM measurements with significantly fewer phase steps because the data only contains the fundamental frequency. However, these large data sets facilitate comparisons of  $\phi^2$ FLIM and conventional homodyne

detection and are used to evaluate the degree of aliasing. In Fig. 7, the  $\phi^2$ FLIM data are fit quite accurately with a function that only includes the fundamental frequency. In contrast, the homodyne data contain multiple harmonics, and functions containing 5 harmonics are insufficient for accurate fitting.

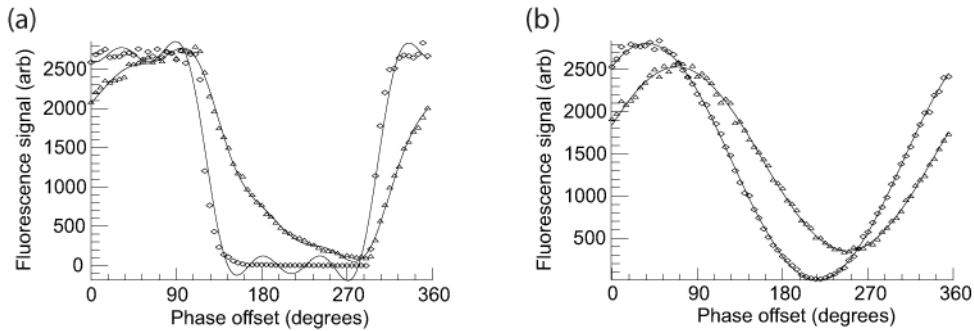


Fig. 7. The measured signals and fitted waveforms for R6G dye in 0.0045 M KI (triangles) and 0.18 M KI (diamonds). These samples correspond to lifetimes of approximately 3.6 ns and 0.7 ns respectively. a) Shows the average data from a 10x10 pixel region for the case of conventional homodyne detection with 5 harmonics fitted, whilst b) shows the same for the  $\phi^2$ FLIM technique, with only one harmonic fitted. With the  $\phi^2$ FLIM technique a single harmonic produces a good fit to the data, indicating that higher harmonics are not present.

### 5.1 System calibration

To verify the accuracy of fluorescence lifetime measurements with the  $\phi^2$ FLIM technique, we compare  $\phi^2$ FLIM results with time-domain fluorescence lifetime measurements in a series of R6G solutions with different quenching rates. Iodide quenching of R6G produces mono-exponential fluorescence decays, which obey a Stern-Volmer relationship, and as such is ideal for system calibration [24]. Figure 8 shows 2D-histograms of the  $AB$  coordinates from five different iodide quenched R6G solutions. The histogram from each sample is normalized by its peak value. The centroid of each histogram is approximately centered along the semi-circle for mono-exponential decays. The fluorescence lifetimes and associated errors for the  $\phi^2$ FLIM measurements of the R6G solutions are calculated using the closest approach algorithm described in Section 4.

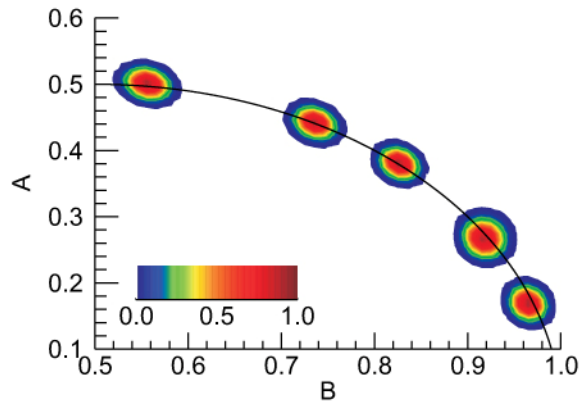


Fig. 8. AB plots for solutions of R6G dye in water with five different concentrations of KI (0.0045 M, 0.027 M, 0.045 M, 0.09 M and 0.18 M) as measured using  $\phi^2$ FLIM.

Time-domain fluorescence lifetime measurements were performed on the same set of R6G solutions. For these measurements, fluorescence was excited by the second harmonic ( $\lambda = 532$  nm) of a regeneratively amplified Nd:YAG laser with a 123 ps FWHM pulse width.

The temporal decay of the fluorescence signal was detected with an MCP photomultiplier tube and recorded on a digital oscilloscope with a 6 GHz bandwidth. The fluorescence traces were fitted to a mono-exponential decay convolved with the instrument response function, which was measured using elastic scattering [25]. Figure 9 shows a Stern-Volmer plot with the inverse of the fluorescence lifetimes,  $1/\tau$ , from both the MCP-PMT and  $\phi^2$ FLIM measurements plotted as a function of potassium iodide concentration, [KI]. The agreement between the two data sets is excellent, and both are a good fit to a straight line, indicating the expected Stern-Volmer behavior. The  $\phi^2$ FLIM measurements give a bimolecular quenching constant  $6.49 \times 10^9 \text{ dm}^3 \text{ mol}^{-1} \text{ s}^{-1}$  and a fluorescence lifetime of 4.0 ns in pure deionized water. These results agree well with values in the literature [12,24].

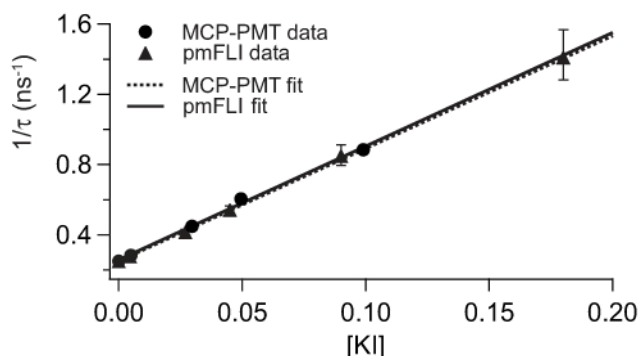


Fig. 9. Stern-Volmer plot comparing time-domain and  $\phi^2$ FLIM lifetime measurements from a series of KI quenched R6G solutions in water.

## 5.2 Aliasing

The ability of the  $\phi^2$ FLIM technique to eliminate aliasing is investigated by comparing lifetime measurements that use different initial phase offsets. If aliasing is present in the data analysis, the measured fluorescence lifetimes will vary as a function of the initial phase offset. We compare the effects of aliasing in the  $\phi^2$ FLIM and conventional homodyne detection schemes. For these comparisons, the full 72-step data sets were sub-sampled to create smaller data sets with different initial phase delays. The  $AB$  plot in Fig. 10(a) shows the mean values and one standard deviation confidence regions for conventional homodyne measurements of the five R6G solutions using 36 phase steps with two different initial phase offsets. For the samples with lower KI concentrations and longer lifetimes, the change in initial phase offset has a negligible effect, and the two results overlap quite well. However, at the highest KI concentration of 0.18M, which corresponds to a fluorescence lifetime of approximately 0.7 ns, the change in the initial phase offset produces a significant shift in the  $AB$  coordinates, indicating that aliasing is a problem. Aliasing is more prevalent for samples with shorter lifetimes because the measurements have higher harmonic content, as demonstrated in Fig. 7. Figure 10(b) shows that the aliasing increases substantially if the sampling is reduced from 36 to 12 phase steps. The discrepancies between the six 12-step measurements for each solution indicate that aliasing is significant for all five samples with very large discrepancies at the shorter lifetimes. For the shortest lifetime, the mean  $AB$  coordinates for the six different phase offsets vary in the ranges (0.96-0.98, 0.09-0.24). The corresponding mean phase lifetime varies between approximately 0.35 ns and 1.0 ns. The aliasing is so severe that the confidence regions for two of the 0.18 M KI samples almost overlap with the confidence regions of the 0.09 M KI samples.

The results for the  $\phi^2$ FLIM measurements are shown in Fig. 11. The close overlap of the six 12-phase step measurements for each of the five samples in Fig. 11(a) indicates that aliasing is completely suppressed for all of the measurements, which is a dramatic improvement over the 12 phase-step conventional homodyne results in Fig. 10(b). Even the

$\phi^2$ FLIM measurements for the solution with the shortest lifetime have negligible aliasing. The ability to perform alias-free FLIM measurements with fewer phase steps is particularly useful when measurement time constraints are an issue. In Fig. 11(b), we evaluate the suppression of aliasing for  $\phi^2$ FLIM measurements using only three phase steps. For clarity of the figure, results from only three of the five R6G solutions are shown in the plot. Although the orientation of the confidence region varies for data sets with different initial phases, the mean  $AB$  coordinate is relatively insensitive to changes in the initial phase. These results indicate that alias-free  $\phi^2$ FLIM measurements are feasible with only three phase steps.

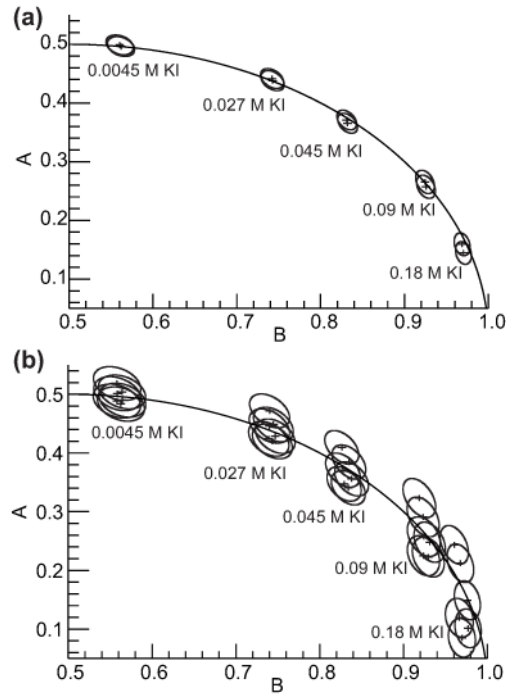


Fig. 10.  $AB$  plots from conventional homodyne detection FLIM measurements, showing the mean and one standard deviation confidence region for samples of R6G dye in water with different KI concentrations. a) Two 36-step data sets with the first phase offset at 0 deg and 5 deg. b) Six 12-step data sets with the first phase offset at 0 deg., 5... 25 deg. If no aliasing is present, the results are independent of the choice of the first phase offset.

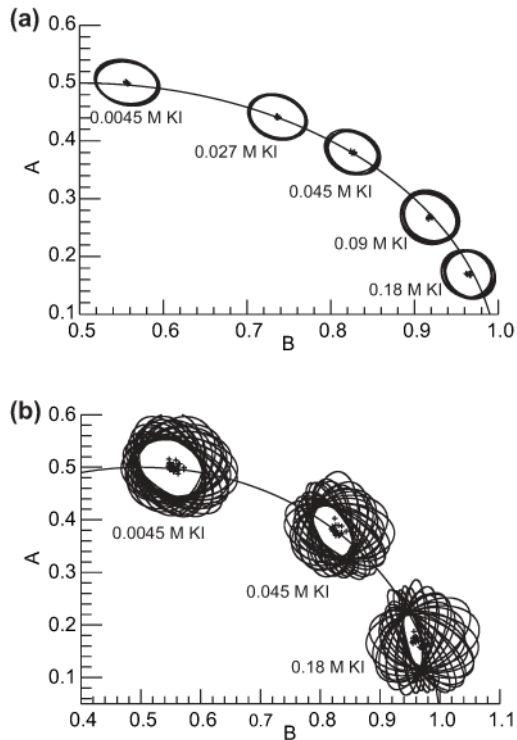


Fig. 11.  $AB$  plots from  $\phi^2$ FLIM measurements, showing the mean values and one standard deviation confidence regions for samples of R6G dye in water with different concentrations of KI, as indicated on the diagrams. a) Six 12-step data sets with the first phase offset at 0 deg., 5...25 deg. b) Twenty-four 3-step data sets with the first phase offset at 0 deg., 5...115 deg.

The suppression of aliasing in the 3 phase-step data for the 0.18 M and 0.0045 M KI solutions is evaluated in more detail in Figs. 12(a) and 12(b), respectively. The plots show the difference between the mean lifetime determined using 3 phase steps and the more accurate lifetime measurement using 72 phase steps. The largest deviations of the mean 3 phase-step measurements are 0.08 ns and 0.12 ns for the 0.71 ns and 3.59 ns lifetimes, respectively. The lack of structure in the distribution of the deviations indicates that there is no systematic bias introduced by aliasing. These results provide validation that the  $\phi^2$ FLIM technique successfully eliminates aliasing.

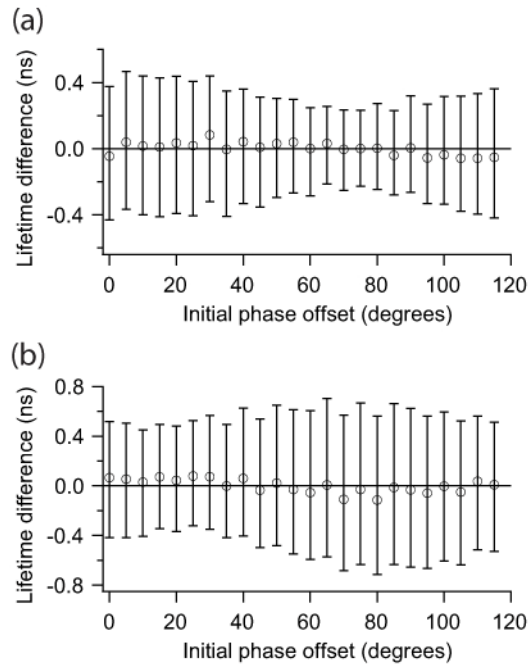


Fig. 12. Dependence of fluorescence lifetime on the initial phase offset for 3 phase-step  $\phi^2$ FLIM measurements. a) R6G solution with a fluorescence lifetime of 0.71 ns b) R6G solution with a fluorescence lifetime of 3.59 ns. The error bars represent one standard deviation of all pixels in an image.

### 5.3 Noise comparison

The  $\phi^2$ FLIM technique provides alias-free fluorescence lifetime measurements with significantly lower noise than the previously published  $\phi$ FLIM technique. Conventional homodyne detection FLIM measurements serve as a standard for noise comparisons. Figure 13 compares the noise levels for  $\phi^2$ FLIM and conventional homodyne detection FLIM measurements. The relative noise in the phase and modulation lifetimes is plotted as a function of  $\omega\tau$ . The full 72 phase-step data sets are used for this comparison to ensure that the homodyne detection measurements are not affected by aliasing. The homodyne detection measurements were performed using the same detector settings as the  $\phi^2$ FLIM measurements with the phase modulation waveform replaced by a constant DC voltage.

The noise levels of the phase and modulation lifetimes are higher for the  $\phi^2$ FLIM measurements than for the conventional homodyne detection measurements. This result is explained by the differences in the modulation depths of the measured signal [19]. The noise increases as the modulation depth decreases. For conventional homodyne detection using a 50% duty cycle square wave, the maximum modulation depth of the fundamental frequency in the measured signal is approximately 1.27 (Eq. (14), whereas it is 1.0 for  $\phi^2$ FLIM (Eq. (18).

These results highlight the tradeoff between  $\phi^2$ FLIM and conventional homodyne detection FLIM. The  $\phi^2$ FLIM method provides alias-free measurements with fewer phase steps, enabling rapid acquisition of  $AB$  images. Fast measurements can be very advantageous if sample movement or photo-bleaching are problematic. However, if time constraints are not an issue, the conventional homodyne detection scheme can provide lower noise measurements and may be preferable as long as enough phase steps can be sampled to resolve higher harmonics. The conventional homodyne detection scheme enables analysis of higher

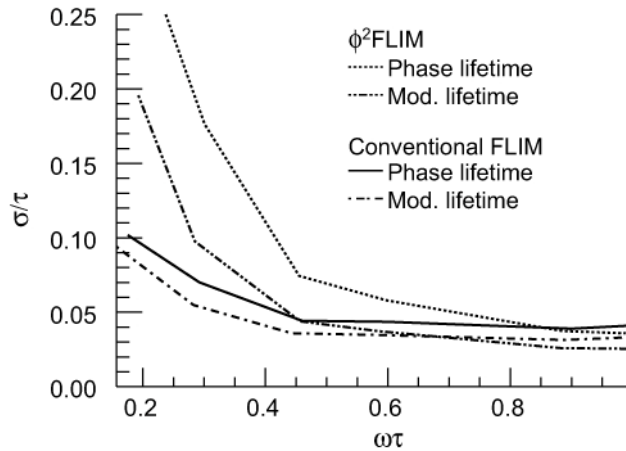


Fig. 13. Comparison of the relative noise,  $\sigma/\tau$ , in the phase and modulation lifetimes as a function of  $\omega\tau$  for conventional homodyne detection and  $\phi^2$ FLIM measurements. The noise is calculated using the full 72 phase-step data sets.

harmonics, which can be used to resolve biexponential decays in a single measurement [13,18]. The choice of the measurement method is a balance between these factors.

#### 5.4 Excitation wavelength resolved $\phi^2$ FLIM imaging

An important issue in fluorescence lifetime detection is the measurement of systems that contain more than one fluorescent component. In these systems, the fractional contribution of each fluorophore to the total fluorescence signal is affected by multiple factors, such as variations in fluorophore concentrations and local quenching rates. The fractional contribution also depends on the excitation and detection wavelengths. Preferential detection of one fluorophore in a multi-component system is feasible if the excitation or emission spectra are significantly different from those of the other fluorophores. Previous studies have varied the bandpass wavelength of the detection system to differentiate emission of two fluorophores [14]. The fixed wavelength lasers that are used in most fluorescence lifetime imaging systems preclude preferential excitation of different fluorophores by tuning the excitation wavelength. Tunable dye laser systems have been used for time-domain FLIM measurements, but the gain curves of the dyes limit the tuning range to 50-100 nm [6]. Ti:Sapphire lasers have also been used for FLIM measurements [26], but access to the full visible spectrum requires harmonic generation, and the cost of these laser systems is significantly greater than a supercontinuum sources. The fluorescence lifetime imaging system in the present study employs a supercontinuum source to provide tunable excitation over the entire visible spectrum. If two fluorophores have significantly different absorption spectra, the relative absorption of each fluorophore can be controlled by selection of the excitation wavelength. Supercontinuum sources have previously been used for time-domain FLIM measurements [27].

In a dual component system, the  $AB$  coordinates for different excitation wavelengths lie along a straight line that connects the  $AB$  coordinates from pure samples of each fluorophore. The principle of excitation wavelength resolved  $AB$  imaging with  $\phi^2$ FLIM is demonstrated in Fig. 14 using a solution of R6G and Rhodamine B (RB) in deionized water. The fluorescence excitation spectra for the individual dyes are shown in Fig. 14(a). The spectra are normalized to the peak signal of R6G and are not corrected for the spectral response of the detection system. The relative concentration of the dyes used for measuring these spectra is the same as that in

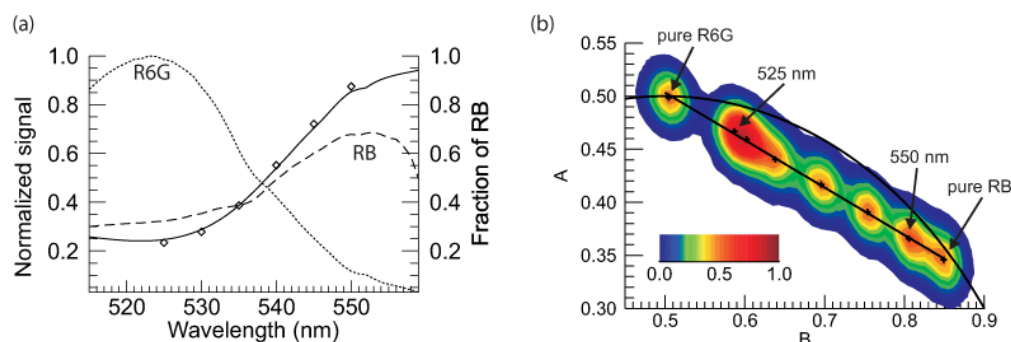


Fig. 14. a) Normalized fluorescence excitation spectra of Rhodamine B (dashed line) and Rhodamine 6G (dotted line). The expected fractional contribution of Rhodamine B to the fluorescence signal (solid line) based on the excitation spectra is plotted as a function of the excitation wavelength. The fractional contribution of RB measured with  $\phi^2$ FLIM is plotted for wavelengths between 525 nm and 550 nm (diamonds). b) Contour plot of the normalized distributions of  $AB$  coordinates for a mixture of 0.5  $\mu$ M Rhodamine B and 0.5  $\mu$ M Rhodamine 6G excited at a series of wavelengths from 525 to 550 nm in 5 nm increments. The mean  $AB$  position for each excitation wavelength is indicated by a cross. The curved solid line is the semi-circle for mono-exponential decays, and the straight solid line is the mixing line for Rhodamine B and Rhodamine 6G.

the mixture solution. The expected fractional contribution of Rhodamine B to the total fluorescence signal from a mixture of the two dyes is calculated from these excitation spectra. We performed  $\phi^2$ FLIM measurements in the dye mixture at a series of excitation wavelengths from 525 to 550 nm. Figure 14(b) shows a contour plot of the distributions of  $AB$  coordinates at different excitation wavelengths. The distribution at each wavelength is normalized by the corresponding peak value.

As the excitation wavelength increases, Rhodamine B is preferentially excited, and the measured  $AB$  coordinate shifts along the line connecting the coordinates for pure R6G and RB. We refer to this line as the mixing line. The  $AB$  coordinate of the mixture is a linear combination of the coordinates of each dye. As a result, the fractional contribution of each dye to the total fluorescence signal is equivalent to the fraction of the distance along the mixing line. The fractional contribution of RB at each excitation wavelength was determined by locating the closest point on the mixing line to the mean  $AB$  coordinate and then calculating the fraction of the distance along the mixing line to this point. The fractional contribution of RB is plotted at six wavelengths in Fig. 14(a). The values measured with  $\phi^2$ FLIM agree very well with the expected values that were calculated from the excitation spectra. These results demonstrate that  $\phi^2$ FLIM can provide quantitative mixing measurements in a two-component fluorescent system. Excitation wavelength resolved  $AB$  plots provide more information than measurements at a single wavelength and have potential as a diagnostic tool for analysis of complicated systems, such as systems with fluorescence resonance energy transfer.

### 5.5 Rapid $\phi^2$ FLIM measurements

Rapid fluorescence lifetime imaging measurements are required for samples with measurement time constraints, such as temporally evolving systems or samples that are susceptible to photo-bleaching. One of the advantages of the  $\phi^2$ FLIM technique is that alias-free fluorescence lifetime measurements can be acquired with as few as three phase steps without compromising precision. This feature enables lifetime imaging at high acquisition rates.

There are several previous examples of FLIM systems with high acquisition rates. Fluorescence lifetime imaging at rates of 12.3 Hz has been demonstrated using time-gated measurements coupled with a rapid lifetime determination (RLD) technique. In the RLD method, fluorescence lifetimes are calculated using only two fluorescence images that are

acquired at different time delays relative to the fluorescence excitation pulse [28]. The two fluorescence images can be collected within the same exposure by using a segmented image intensifier. This approach enables even faster measurements with rates up to 29 Hz at reduced spatial resolution [29]. The detection of fluorophore mixtures requires further segmentation of the detector to sample more points along the fluorescence decay curve [30]. A disadvantage of the RLD time-gated method is that it uses a very limited number of measurements to sample subsections of the fluorescence decay curve. For fluorescence lifetimes on the order of nanoseconds, very short gate times are required, and the signal-to-noise ratio of the measurements decreases with the gate time. Furthermore, the use of segmentation reduces the spatial resolution.

High-speed frequency-domain lifetime imaging was previously demonstrated at a rate of 8 Hz with 300 x 220 pixel images [31]. Lifetime measurements were performed without aliasing problems using a sine function for the excitation waveform and recording only three fluorescence images. However, the use of a sine function reduces the modulation depth and signal-to-noise ratio of the lifetime measurement, as discussed in Section 2. That system provided even faster measurements via the normalized difference method, which measures lifetime differences using only two fluorescence images [9].

The  $\phi^2$ FLIM system in this study is capable of fluorescence lifetime measurements with a resolution of 256 x 256 pixels at rates of up to 5.5 Hz. Each lifetime measurement requires the acquisition of three fluorescence images with different phase offsets. The fluorescence images are thus recorded at rates up to 16.5 Hz. The acquisition rate is limited by the readout time of the CCD camera, which decreases as the pixel resolution is reduced. There is thus an inherent tradeoff between the measurement speed and spatial resolution. To demonstrate rapid  $\phi^2$ FLIM measurements, we imaged drops of RB in a glycerol-water solution falling through abath containing R6G dye in a 40:60 glycerol-water solution. The R6G solution was placed in a cuvette that was 1 cm wide, 0.2 cm deep, and 4 cm high. Drops of the RB dye solution were injected at the top of the cuvette. The cuvette was oriented such that its smallest dimension corresponded to the out-of-plane dimension of the  $\phi^2$ FLIM measurement. The droplet motion was thus confined to a narrow slot, which minimized variation of mixing structures in the out-of-plane direction. The glycerol content of the RB solution was adjusted such that the drops had a slightly higher density than the R6G bath solution. The resulting velocity of the falling drops was approximately 1 mm/s.

The  $\phi^2$ FLIM measurements of the falling drops were analyzed using *AB*-plots. The mixing line for the RB and R6G solutions was determined from measurements of individual samples of the two dye solutions. Figure 15(a) shows *AB*-plots for the two dyes with the mixing line connecting the mean *AB* coordinates of each dye. The departure of the pure RB data from the single-exponential semi-circle may result from the quenching effects of glycerol in the solution. Figure 15(b) shows the distribution of *AB* coordinates from a single  $\phi^2$ FLIM image of a falling RB drop mixing with R6G. The location of the *AB* coordinates along the mixing line is used to determine the fraction of the fluorescence signal from Rhodamine B on a pixel-by-pixel basis. The fraction of RB dye solution in the mixture is then determined by correcting for the relative strengths of the fluorescence signals from the pure solutions of RB and R6G dye solutions. The result is a quantitative imaging measurement of the mixing process, as shown in Fig. 15(c).

Figure 16 shows three frames of the calculated fraction of RB solution from two different image sequences of falling droplets. The corresponding distributions of *AB* coordinates are plotted next to each frame. Each frame was acquired in 182 ms, and the data was smoothed using a Gaussian kernel with a standard deviation of four pixels to reduce the noise. The images show excellent contrast between the two dyes and clearly resolve the rotating vortex structures formed at the boundaries of the droplets. The vortical structures become elongated as the droplets entrain the bath solution. The effects of spatial averaging due to the droplet motion during the acquisition of a single frame of the  $\phi^2$ FLIM measurement are negligible since the drop is convected only 180  $\mu\text{m}$ . The uncertainty in the fraction of RB solution at a

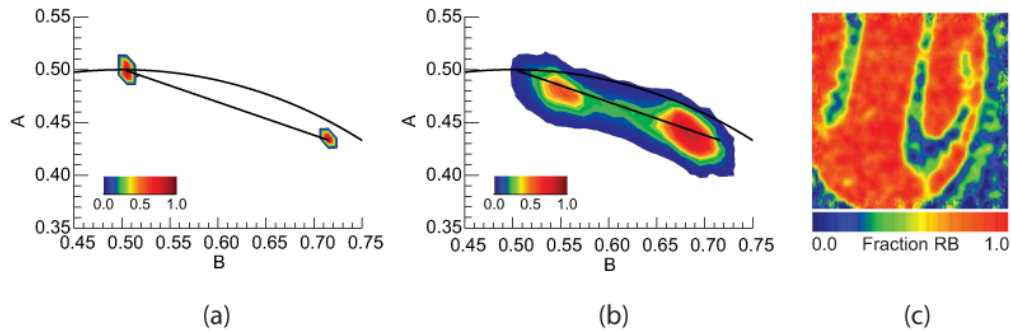


Fig. 15. a)  $AB$ -plot for samples of pure R6G and pure RB in glycerol-water solutions. The mixing line indicates the range of  $AB$  coordinates for all possible mixtures of the R6G and RB solutions. The curve is the mono-exponential decay semi-circle. b) Distribution of  $AB$  coordinates from a  $\phi^2$ FLIM image of a droplet of RB solution mixing with a bath of R6G solution. c) Image showing measured fraction of RB dye solution.

single pixel is approximately  $\pm 0.09$ . The uncertainty is estimated by examining the noise distribution in a region containing only R6G.

The  $AB$ -plots indicate the fraction of each dye solution and the degree of mixing of the dye solutions within each frame. The sequence in Figs. 16(a)-(b) shows a progression of the mixing process. As the droplet of RB enters the field of view in Fig. 16(a), the image is dominated by regions containing R6G. At a later time, Fig. 16(b) shows the majority of the image contains RB and a modest area contains a mixture of both dyes, resulting in intermediate values along the mixing line. Figure 16(c) shows the tail of the vortex with comparable portions of each dye and significant areas with a mixture of the dyes. The increased mixing of the dyes is evident from the filled-in distribution of  $AB$ -coordinates along the mixing line in Fig. 16(c). The sequence of measurements in Figs. 16(d)-(f) show mixing of another drop that has broken up into smaller scale mixing layers. The enhanced mixing results in a more uniform distribution of  $AB$ -coordinates along the mixing line. The  $AB$ -plots thus provide a quantitative measurement of mixing by both stirring motions and diffusion. If mixing only occurs by stirring, the  $AB$ -plot will be bimodal with prominent peaks at the  $AB$ -coordinates corresponding to each of the individual dyes. In contrast, mixing by diffusion results in  $AB$ -coordinates that are distributed along the mixing line.

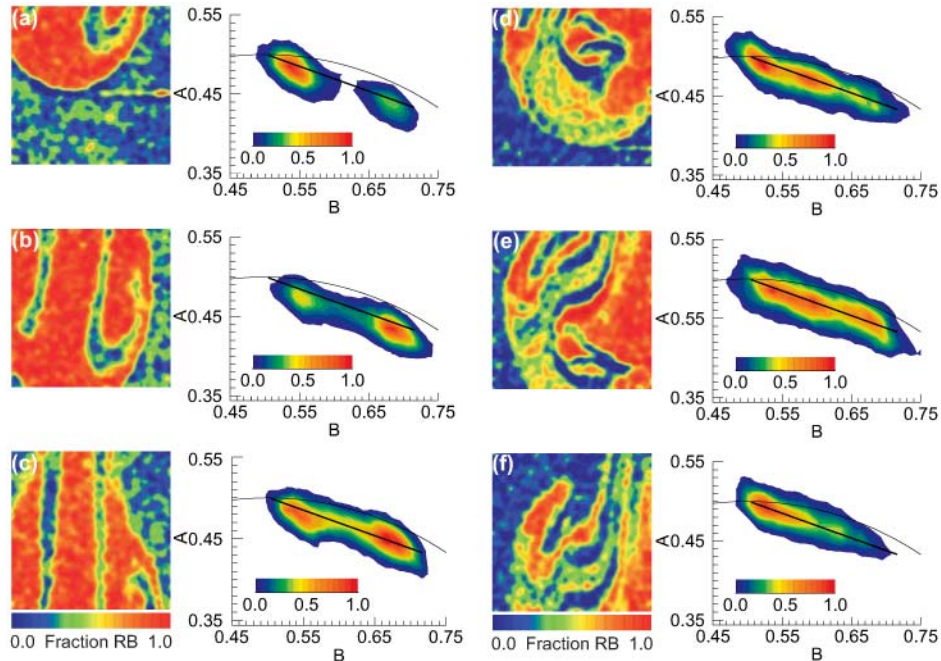


Fig. 16. Sequences of  $\phi^2$ FLIM images show drops of RB in a glycerol/water solution mixing into a bath of R6G in glycerol/water. Sample frames are extracted from  $\phi^2$ FLIM measurements acquired at 5.5 Hz. Frames (a)-(c) show the fraction of RB solution at three times separated by 1.45 s. Frames (d)-(f) show the fraction of RB solution for a second drop with 2.18 s between frames. For each frame, the corresponding  $AB$ -plot shows the distribution of  $AB$ -coordinates along the mixing line.

## 6. Conclusions

We have demonstrated a new method for eliminating aliasing from frequency-domain fluorescence lifetime imaging measurements. The  $\phi^2$ FLIM technique uses phase modulation of the detector gain waveform to provide highly resolved sampling of signals in homodyne FLIM measurements while suppressing higher harmonics. This technique significantly expands the range of excitation sources that can be used for frequency-domain lifetime imaging since the higher harmonics from the excitation source are suppressed. For example, fluorescence excitation can be performed with picosecond pulses, which are approximately Dirac delta functions for fluorescence decay times on the order of nanoseconds. This excitation scheme provides greater signal-to-noise ratios than conventional fd-FLIM measurements.

$\phi^2$ FLIM measurements were demonstrated using a supercontinuum laser as a fluorescence excitation source and a MCP image intensifier with square-wave gain modulation for detection. The suppression of higher harmonics in the detected signal was evaluated with Rhodamine dye solutions. The  $\phi^2$ FLIM method was validated by comparing  $\phi^2$ FLIM and time-domain lifetime measurements in dye solutions with decay times ranging from 0.5 ns to 4.0 ns. Errors due to aliasing were evaluated by comparing  $\phi^2$ FLIM measurements with different initial phase steps. The results show negligible aliasing effects, even when only three phase steps were used. In contrast, fluorescence lifetime measurements using conventional homodyne detection frequency-domain FLIM with twelve phase steps were highly susceptible to aliasing. The susceptibility to aliasing was greatest for samples with short lifetimes because of the higher harmonic content in the detected signal. For lifetimes greater than 1 ns, conventional measurements required 36 phase steps to resolve the majority of the higher harmonics. If collection time is not a constraint, then highly sampled homodyne

detection can provide lifetime measurements with high signal-to-noise ratio, and multi-harmonic analysis is possible.

If measurement time constraints are an issue, conventional homodyne detection with limited phase samples is corrupted by significant aliasing. The  $\phi^2$ FLIM method eliminates aliasing by suppressing higher harmonics in the detected signal and provides lifetime measurements with a signal-to-noise ratio comparable to that of the homodyne detection scheme. The data analysis for both approaches uses the same least squares fitting procedure. The use of *AB*-plots for presenting the results is particularly powerful as it allows easy visualization of fluorescence lifetime measurements. It readily indicates whether fluorescence decays are mono-exponential or multi-exponential and enables quantitative measurements of dye mixing.

The ability to perform frequency-domain FLIM measurements using only 3 phase steps enables rapid lifetime imaging to be performed. This was demonstrated by imaging drops containing RB falling through a solution containing R6G, with lifetime images acquired at a rate of 5.5 Hz. The fraction of RB dye solution was calculated on a pixel-by-pixel basis using the *AB*-plot analysis. Faster imaging rates may be possible using a segmented image intensifier [29]. The use of a supercontinuum source enabled excitation wavelength resolved lifetime imaging. This capability significantly expands the characterization of samples containing mixtures of fluorophores, which is particularly important in microscopy applications. We demonstrated the use of *AB*-plots for quantitative analysis of mixing of dye solutions.

The system developed here offers a new capability for lifetime imaging applications. If imaging time is unconstrained, then conventional homodyne detection can be employed by using a DC waveform for phase modulation, allowing optimal signal-to-noise as well as multi-harmonic data analysis [18]. However, when imaging time is constrained, the  $\phi^2$ FLIM technique can be used by applying the appropriate phase modulation waveform. Lifetime images can be acquired with as few as three phase steps, while retaining comparable signal-to-noise ratios. In combination with excitation resolved imaging and *AB*-plot analysis, this provides a powerful tool for the analysis of systems with a mixture of fluorophores.

### **Acknowledgments**

The authors thank Dr. C. C. Hayden of Sandia National Laboratories for valuable discussions and M. Gutzler for expert technical assistance. This research was supported by the U.S. Department of Energy, Office of Basic Energy Sciences, Division of Chemical Sciences, Geosciences, and Biosciences. Sandia National Laboratories is a multiprogram laboratory operated by Sandia Corporation, a Lockheed Martin Company, for the U.S. Department of Energy under contract DE-AC04-94-AL85000. Support was also provided by the EPSRC (EP/F033176/1 and EP/F028261/1) and the BBSRC (BB/E008542/1).